The limiting hole pressure in three dimensions[☆]

Vasileios Symeonidis [a], Bruce Caswell [b],*

[a] *Division of Applied Mathematics, Brown University, Providence, RI 02912, United States*
[b] *Division of Engineering, Brown University, Providence, RI 02912, United States*

Abstract

The three-dimensional analog of the Giesekus–Tanner (G–T) theorem [B. Caswell, Non-Newtonian flow at lowest order: the role of the Reiner-Rivlin stress, J. Non-Newtonian Fluid Mech. 133 (1) (2006) 1–13] allows the flow in the vicinity of a pressure tap to be analyzed with the solution of the inertialess flow of a Reiner-Rivlin fluid just as G–T was used [R.I. Tanner, A. Pipkin, Intrinsic errors in pressure-hole measurements, Trans. Soc. Rheol. 14 (1969) 471] to analyze the corresponding two-dimensional flow with the Stokes solution. Later Kearsley [E.A. Kearsley, Intrinsic errors for pressure measurements in a slot along a flow, Trans. Soc. Rheol. 14 (3) (1970) 419–424] extended the Tanner–Pipkin analysis to the rectilinear flow in a channel with a parallel slot. In the two-dimensional case the Tanner–Pipkin term is the hole pressure relative to the Stokes value (usually neglected), and is determined solely by the first normal stress function evaluated at the wall shear rate of the undisturbed flow. It is thus "intrinsic" since dimensional analysis suggests the hole pressure should also depend on the hole geometry. Kearsley's result is independent of slot geometry only in the limit that the slot is deep and very narrow relative to the size of the main channel. In three-dimensions the Tanner–Pipkin term again contributes an intrinsic pressure independent of hole geometry, but now it is now relative to the Reiner–Rivlin value which itself depends on the hole geometry and is not negligible. Hence the complete hole pressure in three-dimensions requires the solution of the Reiner–Rivlin problem which in general will be obtained numerically. The latter is formulated for numerical simulation so that the hole pressure can be read off from values of the pressure field without any post-processing calculation of velocity gradients. The numerical simulations were performed with a three-dimensional spectral element code [G.E. Karniadakis, S.J. Sherwin, Spectral/*hp* Element Methods for CFD, Oxford University Press, 1999] well suited to the efficient solution of flow problems in complex geometries. The limiting values of the Reiner–Rivlin hole pressure have been obtained for several hole/channel ratios. Numerical results for the larger holes are not in agreement with the H–P theory [K. Higashitani, W.G. Pritchard, A kinematic calculation of intrinsic errors in pressure measurements made with holes, Trans. Soc. Rheol. 16 (4) (1972) 687–696], and for such holes the Stokes hole pressure was found to be in the measurable range.

1. Stress in materially steady flows

In a previous article Caswell [1] defined the materially steady stress system in terms of the Reiner–Rivlin stress system which in isochoric flow is an isotropic function of **A**, twice the strain rate tensor, and is given by

$$\mathbf{R} = -\mathbf{1}P(II, III) + \eta(II, III)\mathbf{A} + \alpha(II, III)\mathbf{A}^2 \qquad (1)$$

Here the scalar coefficients η and α are functions of II and III, the second and third invariants of **A** defined by

$$II = \tfrac{1}{2}\,\mathrm{tr}\,\mathbf{A}^2, \qquad III = \tfrac{1}{3}\,\mathrm{tr}\,\mathbf{A}^3 \qquad (2)$$

The isotropic scalar pressure P is an arbitrary function of which a part may be expressed in terms of II and III and another part is to be determined by the solution of the equation of motion and the boundary conditions which define the flow problem.

Caswell [1] defines the materially steady stress **S** in terms of the Reiner–Rivlin stress **R** of Eq. (1), including the scalar pressure P, as

$$\mathbf{S} = \mathbf{R} - \frac{\mathcal{D}(\lambda(II, III)\mathbf{R})}{\mathcal{D}t + \mathbf{1}\Psi} \qquad (3)$$

---

where λ is a scalar function of the indicated arguments, and $\mathbf{\Psi}$ is an additional isotropic stress which may be required to satisfy the equation of motion. The co-rotational time rate is denoted by $\mathcal{D}(*)/\mathcal{D}t$, and is clearly distinguishable from the material derivative denoted by an over dot. In steady viscometric flows $III = 0$, and the coefficients η, α and the factor λ are then functions of II alone. It is easily shown that Eq. (3) becomes the familiar CEF equation [2] with viscosity function $\eta(II)$, first normal stress coefficient $2\lambda(II)\eta(II)$ and second normal stress coefficient $\alpha(II) - \lambda(II)\eta(II)$.

Caswell [1] gave dynamical arguments for requiring two of the coefficients in Eq. (3) to be derivable from a strain-rate potential $\Phi(II, III)$ with the time-function $\lambda(II, III)$ as an integrating factor. Theorem 1.1 below, restricts λ to be constant and replaces Φ with $\lambda\phi(II, III)$. The significance of the potential $\phi(II, III)$ is that its volume integral is the functional to be rendered stationary in the variational formulation [3] of the inertialess Reiner–Rivlin problem,

$$\nabla \cdot \mathbf{V} = \mathbf{0}, \qquad \nabla \cdot \mathbf{R} = \mathbf{0}, \qquad \nabla \times (\nabla \cdot \mathbf{R}') = \mathbf{0}, \tag{4}$$

where $\mathbf{R}'$ is the non-isotropic part of the Reiner–Rivlin stress equation (1) whose coefficients are given by

$$\eta = \frac{\partial\phi}{\partial II}, \qquad \alpha = \frac{\partial\phi}{\partial III}. \tag{5}$$

Caswell [1] summarizes the role of the Reiner–Rivlin stress in flows governed by the materially constant stress of Eq. (3) with constant λ as follows:

Theorem 1.1. *Let* $\mathbf{V}$, *P be velocity, pressure fields, and let* $\mathbf{S}$ *be the materially constant stress of* Eq. (3) *with constant λ and with* $\mathbf{\Psi} = \lambda\phi(II, III)/2$,

$$\mathbf{S} = \mathbf{R} - \lambda\left[\frac{\mathcal{D}\mathbf{R}}{\mathcal{D}t} - \frac{1}{2}\phi(II, III)\right] \tag{6}$$

where $\mathbf{R}$ *is constructed from* $\mathbf{V}$, *P with* Eq. (1). *Then this stress system satisfies the inertialess flow or equilibrium equation and its compatibility condition on the non-isotropic part* $\mathbf{S}'$ *of* $\mathbf{S}$,

$$\nabla \cdot \mathbf{S} = \mathbf{0}, \qquad \nabla \times (\nabla \cdot \mathbf{S}') = \mathbf{0}, \tag{7}$$

provided the velocity–pressure fields $\mathbf{V}$, *P satisfy the Reiner–Rivlin problem of* Eq. (4) *with coefficients* $\eta(II, III)$, *$\alpha(II, III)$ derivable from the strain-rate potential $\phi(II, III)$ according to* Eq. (5).

Tanner [4] proved a similar theorem for flows governed by the equilibrium of the CEF stress in the two-dimensional plane where $III = 0$, α plays no role and η is a function of II alone. In the limit of small strain rates, II, $III \to 0$ the coefficients η, α of Eq. (1) are constants, λ is the mean relaxation time of linear viscoelasticity, and the strain-rate potential becomes

$$\phi = \eta II + \alpha III \tag{8}$$

Theorem 1.1 reduces to Theorem 1a of Caswell [1], the three-dimensional generalization of the Giesekus–Tanner (G–T) theorem [5,6]. The materially steady stress system (6) then

becomes the augmented second order fluid,

$$\mathbf{S} = -\mathbf{1}\left[P - \lambda\dot{P} - \lambda\eta\frac{II}{2} - \lambda\alpha\frac{III}{2}\right] + \eta\mathbf{A}$$
$$+ \alpha\mathbf{A}^2 - \lambda\eta\frac{\mathcal{D}\mathbf{A}}{\mathcal{D}t} - \lambda\alpha\frac{\mathcal{D}\mathbf{A}^2}{\mathcal{D}t}. \tag{9}$$

This stress system is the complete second order fluid (SOF) system with three coefficients augmented by the last term of third order whose coefficient is a product of two coefficients of the SOF. The G–T theorem is recovered either by setting $\alpha = 0$ in Eqs. (8) and (9), or by restriction of the motion to plane flow where $\mathbf{A}$ is isotropic and the terms in α can be absorbed into the isotropic pressure. With $\alpha = 0$ and constant η the Reiner–Rivlin stress $\mathbf{R}$ of Eq. (1) reduces to the Newtonian stress, and the Reiner–Rivlin problem of Eq. (4) becomes the Stokes problem. The power of G–T theorem is the prospect of obtaining the solution of a nonlinear problem from that of the corresponding linear one. Theorem 1a of [1] shows that in three-dimensions all that can be expected is a reduction of the order of spatial differentiation, which can have important advantages when numerical solutions are sought. It is clearly preferable to apply numerical methods to a problem defined by Eq. (4) instead of Eq. (7). This is the basis for the calculation of the limiting value of the three-dimensional hole pressure, which is the main objective of this paper.

2. The hole pressure

A tap in the wall of a channel, Fig. 1, gives rise to a small flow disturbance which in turn alters the pressure relative to its undisturbed value in the neighborhood of the tap. Deep within the hole this disturbance is known as the hole pressure, and is defined by Lodge and Vargas [7] as the difference of the normal tractions $\sigma_w = -P_1$ at the wall in undisturbed channel flow, and $\sigma_h = -P_2$ at the bottom of the hole respectively.

$$P_H = \sigma_w - \sigma_h \tag{10}$$

The depth is large enough to guarantee hydrostatic conditions so that by Eqs. (1) and (9) it follows respectively that both the **R**-
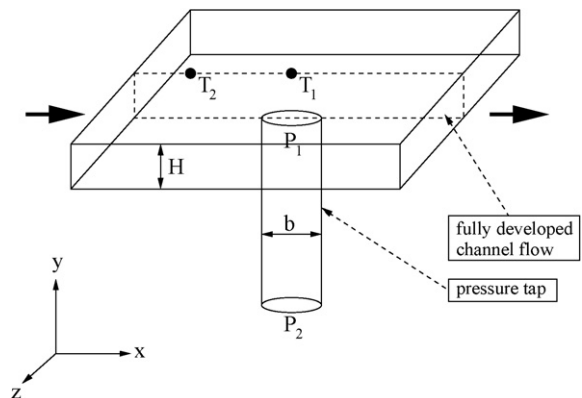

Fig. 1. Channel with pressure tap. T_1 and T_2 indicate locations of pressure transducers in the stressmeter of Lodge and Vargas [7].

stress and the **S**-stress become isotropic. The formal calculation of P_H is carried out in two steps:

1. **S** − **R**, the stress relative to the Reiner–Rivlin stress, is obtained from Eq. (3), and will be shown to be independent of hole size.
2. The part which can be found only by solution of the Reiner–Rivlin problem and depends on the hole size.

The first step requires only that **S** − **R** be considered. Far upstream in the channel the flow is exactly viscometric, and the stress is then given exactly by the materially constant stress of Eq. (3) which reduces to the CEF [2] equation in such flows. Let the velocity be $\mathbf{V} = u(y)\mathbf{i}$ relative to Cartesian coordinates x, y along and transverse to the streamlines respectively, and with z normal to the xy plane. The kinematical tensors of the materially constant stress system are evaluated in terms of the strain rate $\dot{\gamma} = \mathrm{d}u/\mathrm{d}y$ as follows:

$$\mathbf{A} = (\mathbf{ji} + \mathbf{ij})\dot{\gamma}, \qquad \mathbf{A}^2 = (\mathbf{ii} + \mathbf{jj})\dot{\gamma}^2,$$

$$\frac{\mathcal{D}\mathbf{A}}{\mathcal{D}t} = (\mathbf{jj} - \mathbf{ii})\dot{\gamma}^2, \qquad \frac{\mathcal{D}\mathbf{A}^2}{\mathcal{D}t} = 0, \tag{11}$$

and the invariants II, III are then $\dot{\gamma}^2$, 0 respectively. The stress system of Eq. (1) is then

$$\mathbf{R} = -\mathbf{1}p + (\mathbf{ji} + \mathbf{ij})\tau + (\mathbf{ii} + \mathbf{jj})\sigma, \tag{12}$$

and from Eq. (3), **S** − **R** becomes

$$\mathbf{S} - \mathbf{R} = \mathbf{1}(\lambda u p_x + \Psi) - \tfrac{1}{2}N_1(\dot{\gamma}^2)(\mathbf{jj} - \mathbf{ii}),$$

$$\Psi = \tfrac{1}{2}N_1(\dot{\gamma}^2) - \lambda u p_x \tag{13}$$

where $p_x = \frac{\partial p}{\partial x}$, $\tau = \eta\dot{\gamma}$, $\sigma = \alpha\dot{\gamma}^2$, $N_1 = 2\lambda\eta\dot{\gamma}^2$ is the first normal stress difference, and the coefficients η, α, and λ are now functions of II alone. The scalar Ψ is not known for general flows; however, in Appendix A of Caswell [1] it was shown that the form given in Eq. (13) holds in viscometric flow. The disturbance flow due to the hole is not easily calculated by direct solution of the equilibrium equation for typical constitutive equations. The materially constant stress (3) gives an approximate description of the stress in this nearly viscometric flow. However, the higher order spatial derivatives in Eq. (3) are well-known to be troublesome in numerical simulation. Hence a further simplification is required to yield a tractable numerical problem. The approximation of the time function $\lambda(II, III)$ by a constant λ_c reduces the flow problem by means of Theorem 1.1 to the solution of the lower-order Reiner–Rivlin problem (4). It is well-known that with the same viscosity function the CEF problem and the Reiner–Rivlin problem are satisfied by the same viscometric velocity field. This suggests the constant λ_c can be fixed in the far-upstream, viscometric region of the channel by equating, at the channel-wall, the exact difference-stresses of Eq. (13) to the values given by the constant-λ approximation of Eq. (6). By use of Eqs. (11) and (12) the Reiner–Rivlin stress is

constructed, and is substituted into Eq. (6) to yield

$$\mathbf{S} - \mathbf{R} = \mathbf{1}\lambda_c\left(up_x + \frac{\phi}{2} + \frac{\phi_c}{2}\right) - \lambda_c\eta\dot{\gamma}^2(\mathbf{jj} - \mathbf{ii}), \tag{14}$$

where ϕ_c is a constant which has no effect on the equilibrium equation (7), and the potential $\phi(\dot{\gamma}^2, 0)$ vanishes as $\dot{\gamma}^2 \to 0$. In viscometric flow Caswell [1](see Appendix A therein) showed that ϕ can be expressed in terms of the shear stress τ as

$$\frac{\phi(\tau)}{2} = W_R(\tau) - \int_0^\tau \frac{W_R(\tau')}{\tau'}\,\mathrm{d}\tau', \qquad W_R = \tau\dot{\gamma} \tag{15}$$

Eqs. (13) and (14) have no off-diagonal components, and equality of their corresponding diagonal-components is satisfied by

$$\frac{\phi_c}{2} = \int_0^{\tau_w} \frac{W_R(\tau)}{\tau}\,\mathrm{d}\tau, \qquad \lambda_c = \frac{N_1(\tau_w)}{2\tau_w\dot{\gamma}_w}, \tag{16}$$

where the subscript w denotes wall values in the viscometric domain far from the hole. Hydrostatic conditions at the bottom of a deep hole means the only non-zero term in Eq. (6) is the constant isotropic tension, hence

$$\mathbf{S} - \mathbf{R} = \mathbf{1}\frac{\lambda_c\phi_c}{2} = \mathbf{1}\int_0^{\tau_w} \lambda_c\frac{W_R(\tau)}{\tau}\,\mathrm{d}\tau. \tag{17}$$

Lodge and Vargas [7] define the *hole pressure* as the wall value of the normal wall-stress in undisturbed plane Poiseuille flow minus the total stress deep inside the hole. From Eqs. (14) and (16) the **jj**-component of the difference stress is zero on the wall, and hence the hole pressure in excess of the Reiner–Rivlin value is, in fact, the isotropic stress in Eq. (17). Tanner [4] obtained this integral in plane flow with the assumption that the first normal stress coefficient is proportional to the viscosity function. As suggested above, this term is intrinsic, i.e. independent of the hole geometry. In the limit of small strain rates Theorem 1.1 reduces to Theorem 1a of [1], λ_c becomes the mean relaxation time of linear viscoelasticity and the integral (17) goes to the Pipkin-Tanner [8] limit of $N_1/4$.

The complete hole pressure is obtained in step 2 by solution of the Reiner–Rivlin problem in the channel-with-hole geometry (Fig. 1). In the formulation of the Reiner–Rivlin problem given below the pressure is modified so that Eq. (1) is replaced by

$$\mathbf{R} = -\mathbf{1}P + \eta\mathbf{A} + \alpha(\mathbf{A}^2 - \mathbf{1}II) \tag{18}$$

The effect of this pressure definition is that in plane flow the α term vanishes. In viscometric flow the stress component normal to the shear planes is $-P$, and since the pressure is a primitive variable in the numerical scheme the hole pressure given by Eq. (10) can be read off from the solution without spatial differentiation of the velocity field. In this work solutions have been obtained only for the small strain-rate limit where η and α are constant, and where dimensional analysis suggests the Reiner–Rivlin hole pressure P_{RR} should have the form

$$P_{RR} = -P_{HS} - r\alpha\dot{\gamma}_w^2, \tag{19}$$

where the Stokes ($\alpha = 0$) hole pressure P_{HS} and r are constant for every hole size. As defined, r is positive for all known cases. These are: $r = 0$, 1/2, 1/6 respectively for the transverse

slot [8], the parallel slot [9], and the circle (Higashitani and Pritchard [10]). The flow across the transverse slot is planar, and hence r is zero since the α-term vanishes from Eq. (18). Kearsley [9] showed that with a modified pressure field the velocity field for the rectilinear flow of a Newtonian fluid also satisfies the Reiner–Rivlin problem. The flow in the parallel slot is an example of a rectilinear motion, and it is used in this work as a benchmark for the numerical method. From Eqs. (10), (17) and (19), the total hole pressure in the limit of small strain rates can be written as

$$P_{\mathrm{H}} = \frac{N_1}{4} + P_{\mathrm{RR}} = \frac{N_1}{4} - r\left[\frac{N_1}{2} + N_2\right] - P_{\mathrm{HS}}, \tag{20}$$

where N_1 and N_2 are the first and second normal stress differences respectively.

The use of the augmented SOF, Eq. (9), for the flow near the hole can be questioned on the grounds that while velocity gradients over most of the domain can be small those in the vicinity of sharp corners can become very large. This applies equally to the plane flow result of Tanner and Pipkin [8] for the hole pressure due to a transverse slot, the first term of Eq. (20). Along the center plane, $z = 0$, of Fig. 1. the flow near the rim of the hole should resemble the plane flow in the vicinity of re-entrant corners which is known to give rise to singular, but integrable stress fields for the Newtonian case. Since the nonlinear term in Eq. (18) vanishes in plane flow its effects should be minimal near such points of symmetry. In the center plane $x = 0$ of Fig. 1, the flow at the rim points connecting the cross-flow hole diameter should locally resemble Kearsley's rectilinear channel flow. In the numerical investigations of this work both sharp and rounded corners were tried, and the calculated r values were found not to be greatly affected.

3. The Reiner–Rivlin stress in nearly incompressible flows

In plane flows the Cayley–Hamilton theorem takes the form

$$\mathbf{A}^2 - [\mathrm{tr}\,\mathbf{A}]\mathbf{A} + [\tfrac{1}{2}(\mathrm{tr}\,\mathbf{A})^2 - II]\mathbf{1} = \mathbf{0}, \tag{21}$$

where $\mathrm{tr}\,\mathbf{A} = 2\nabla\cdot\mathbf{V}$. It follows from Eq. (21) that for plane isochoric motions the flows of the Reiner–Rivlin fluid (Eq. (18)) are indistinguishable from the corresponding flows of a Newtonian fluid with viscosity η. In numerical simulation incompressibility is nearly always imposed as a constraint, and consequently the calculated flow fields are nearly, but not exactly, isochoric. It is of interest to formulate the Reiner–Rivlin stress so that the α-term in Eq. (18) will produce dynamic effects only in three-dimensional flows regardless of compressibility. Since incompressibility is imposed as part of the solution of the equilibrium equation (4) the Reiner–Rivlin stress is formulated in terms of $\mathbf{A}$ modified by any multiple of $\nabla\cdot\mathbf{V}$. In terms of $\mathbf{B} = \mathbf{A} - (\nabla\cdot\mathbf{V})\mathbf{1}$ it is easily shown that the left hand side of Eq. (21) becomes

$$\mathbf{B}^2 + \tfrac{1}{2}[(\mathrm{tr}\,\mathbf{B})^2 - \mathrm{tr}(\mathbf{B}^2)]\mathbf{1} - (2 - \mathrm{tr}\,\mathbf{1})(3 - \mathrm{tr}\,\mathbf{1})(\mathrm{tr}\,\mathbf{B})^2\mathbf{1}, \tag{22}$$

where the last term obviously vanishes in two or in three dimensions. By design, $\mathrm{tr}\,\mathbf{B}$ is zero in plane flow, and since the whole expression is also zero then $\mathbf{B}^2$ is isotropic in plane compressible flows just as $\mathbf{A}^2$ is isotropic in plane incompressible flows. With the pressure modified by $1/2[(\mathrm{tr}\,\mathbf{B})^2 - \mathrm{tr}(\mathbf{B}^2)]$ the Reiner–Rivlin stress (Eq. (1)) is written with $\mathbf{A}$ replaced by $\mathbf{B}$, as

$$\mathbf{R} = -\mathbf{1}p + \eta\mathbf{B} + \alpha\mathbf{C}, \qquad \mathbf{C} = \mathbf{B}^2 + \tfrac{1}{2}[(\mathrm{tr}\,\mathbf{B})^2 - \mathrm{tr}(\mathbf{B}^2)]\mathbf{1}. \tag{23}$$

In principle, the solution of the dynamical equations rendered under an incompressibility constraint should yield essentially the same numerical result for the stress systems of Eqs. (1) or (23). Numerical experiments on the parallel slot geometry have demonstrated that formulation (23) results in greater accuracy and improved convergence with respect to the magnitude of α.

In the numerical implementation described below $\mathbf{C}$ is calculated from known velocity fields from its Cartesian components displayed in Appendix A. After a Galerkin projection onto element nodes these values are used to obtain $\nabla\cdot\mathbf{C}$ and $\nabla\cdot(\nabla\cdot\mathbf{C})$ which appear in the momentum and pressure equations respectively. Analytical expressions for the direct computation of these quantities are derivable by use of the following identities for the components of the strain rate $\mathbf{A}$:

$$a_{ij} = v_{i,j} + v_{j,i} = \varepsilon_{jik}\omega^k + 2v_{j,i} = \varepsilon_{ijk}\omega^k + 2v_{i,j},$$
$$\omega^k = \varepsilon^{kmn}v_{n,m}. \tag{24}$$

Here ε_{ijk} is the alternator and the ω^k are the components of the vorticity vector $\boldsymbol{\omega}$. When these identities are employed in the definition of $\mathbf{B}$, the components of $\mathbf{C}$, constructed from Eq. (23), can be expressed in the form

$$C_i^k = -\omega^k\omega_i + 2(v_{,i}^j v_{,j}^k + v_i^{,j}v_j^{,k} - v_{,j}^j a_i^k)$$
$$\quad - 2\delta_i^k(v_{,k}^j v_{,j}^k - v_{,j}^j v_{,k}^k), \tag{25}$$

where δ_i^k is the Kronecker delta. Eq. (A.5) of Appendix A are recovered when the components (25) are written in Cartesian coordinates. The vorticity product terms are easily identifiable, and it then follows that the remaining terms appear in Eq. (A.5) as sums of 2×2 Jacobians. The divergence of $\mathbf{C}$ can be derived from Eq. (25) and expressed in condensed notation as

$$\nabla\cdot\mathbf{C} = -\boldsymbol{\omega}\cdot\nabla\boldsymbol{\omega} - 2\nabla\times(\nabla\mathbf{V}\cdot\boldsymbol{\omega}), \tag{26}$$

which is easily shown to vanish in any plane flow independent of the magnitude of $\nabla\cdot\mathbf{V}$. From Eq. (26) the divergence of $\nabla\cdot\mathbf{C}$ is

$$\nabla\cdot(\nabla\cdot\mathbf{C}) = -\nabla\boldsymbol{\omega}:\nabla\boldsymbol{\omega}. \tag{27}$$

Although Eq. (27) is derived from Eq. (26) by an additional spatial differentiation the highest order of differentiation of the velocity field is the same in each, and again this result is independent of the magnitude of $(\nabla\cdot\mathbf{V})$.

4. Numerical method

The momentum equation for the Reiner–Rivlin fluid with constant coefficients takes the dimensionless form

$$\frac{\partial \mathbf{u}}{\partial t} + \mathrm{Re}[\mathbf{u} \cdot \nabla \mathbf{u}] = -\nabla p + \nabla^2 \mathbf{u} + \alpha' \nabla \cdot \mathbf{C} + \mathbf{F}, \qquad (28)$$

where $\mathbf{F}$ denotes the body force vector, $\mathbf{u}$ the velocity vector and $\mathbf{C}$ is defined by Eq. (23). The Reiner–Rivlin number

$$\alpha' = \frac{\alpha \dot{\gamma}_\mathrm{w}}{\eta} \qquad (29)$$

is a Deborah number which measures the strength of the non-Newtonian stress contribution. The Reynolds number $\mathrm{Re} = (\dot{\gamma}_\mathrm{w} b H \rho)/4\eta$ measures the inertial disturbance due to the hole of diameter b. In view of Theorem 1.1 the Reynolds number will be set to zero in all the simulations presented below. The solution is obtained by marching in time to the steady state from a known initial state, and hence the scale of the dimensionless time t is determined by the magnitude of the time step.

4.1. Temporal discretization

For the *temporal discretization* of the Navier–Stokes equations we use a time-splitting stiffly-stable scheme, which enhances stability through backwards differentiation. The implemented scheme has three steps and it is a small extension of the high-order splitting scheme proposed in [11]:

1. Nonlinear step:

$$\hat{\mathbf{u}} = \sum_{q=0}^{J_u-1} \alpha_q \mathbf{u}^{n-q} + \Delta t \sum_{q=0}^{J_u-1} \beta_q$$
$$\times [-Re(\mathbf{u}^{n-q} \cdot \nabla)\mathbf{u}^{n-q} + \alpha' \nabla \cdot (\mathbf{C})^{n-q} + F^{n-q}]. \qquad (30)$$

In the above notation $J_u \in \{1, 2, 3\}$ is the extrapolation order for the velocity field, n is the current time step, α_q, β_q are coefficients associated with the stiffly-stable scheme [11] as shown in Table 1.

2. Pressure step:

$$\nabla^2 p^{n+1} = \nabla \cdot \left(\frac{\hat{\mathbf{u}}}{\Delta t} \right), \qquad (31)$$

Table 1
Coefficients α_q, β_q, γ_0 associated with the stiffly-stable scheme

Coefficient	First order	Second order	Third order
γ_0	1	3/2	11/6
α_0	1	2	3
α_1	0	−1/2	−3/2
α_2	0	0	1/3
β_0	1	2	3
β_1	0	−1	3
β_2	0	0	1

with the momentum-conservation boundary condition

$$\frac{\partial p^{n+1}}{\partial n} = \mathbf{n} \cdot \left[\hat{\mathbf{u}} - \sum_{q=0}^{J_p-1} \beta_q \nabla \times (\nabla \times \mathbf{u}^{n-q}) \right], \qquad (32)$$

except on parts of the boundary where p is specified.

3. Viscous step:

$$\left[\nabla^2 - \frac{\gamma_0}{\Delta t} \right] \mathbf{u}^{n+1} = -\frac{\gamma_0}{\Delta t} \hat{\mathbf{u}} + \gamma_0 \nabla p^{n+1} \qquad (33)$$

In the above notation $J_p \in \{1, 2, 3\}$ is the extrapolation order for the pressure. Dictated by J_u, J_p, the overall temporal accuracy of the scheme can reach third-order for the Newtonian case [11]. The results presented in this work use $J_u = J_p = 2$.

4.2. Spatial discretization

For *spatial discretization* we have adopted the spectral/hp element method described in [12]. It employs standard unstructured and hybrid grids unlike previous approaches that require special structured grids. This new version of spectral elements uses Jacobi polynomials with mixed weights as its hierarchical basis. It accommodates accurate numerical quadrature and flexibility in discretization by employing *polymorphic subdomains*. The degenerate case corresponds to a linear finite element discretization with the vertices corresponding to linear modes. Each element consists of N modes per direction but no gridding within the element is required as all computations are done in modal space. Specifically, each element is separated into linear vertex modes, edge modes, face modes and interior or bubble modes.

For a smooth solution, the error in a Galerkin projection of a smooth function converges exponentially fast to zero by simply increasing the number of modes per element/subdomain. This allows for selective refinement and sharp *a priori* error estimates in the numerical solution without the overhead cost associated with re-generation of a three-dimensional mesh. Another distinction with other versions of the *hp* finite element method that employ monomials is that very high orders can be readily employed (e.g., $N = 32$), and that the multi-dimensional basis is a tensorial product in the transformed domain, [12]. This, in turn, leads to good efficiency in simulations with high-order N. The new method has been implemented in the two- and three-dimensional serial and parallel versions of the computer code named $\mathcal{N}\varepsilon\kappa\mathcal{T}\alpha r$ [13].

5. Convergence studies

5.1. Nonlinear discontinuities at element boundaries

The nonlinear dependence of the Reiner–Rivlin stress, Eq. (23), on the velocity gradient introduces an additional discontinuity across elemental boundaries whose strength is determined by the Deborah number α'. Here the loss of accuracy of the computed solution due to the extra discontinuous terms is investigated by means of a simple, but non-trivial, exact solution of the governing equations. An exact solution of the inertialess
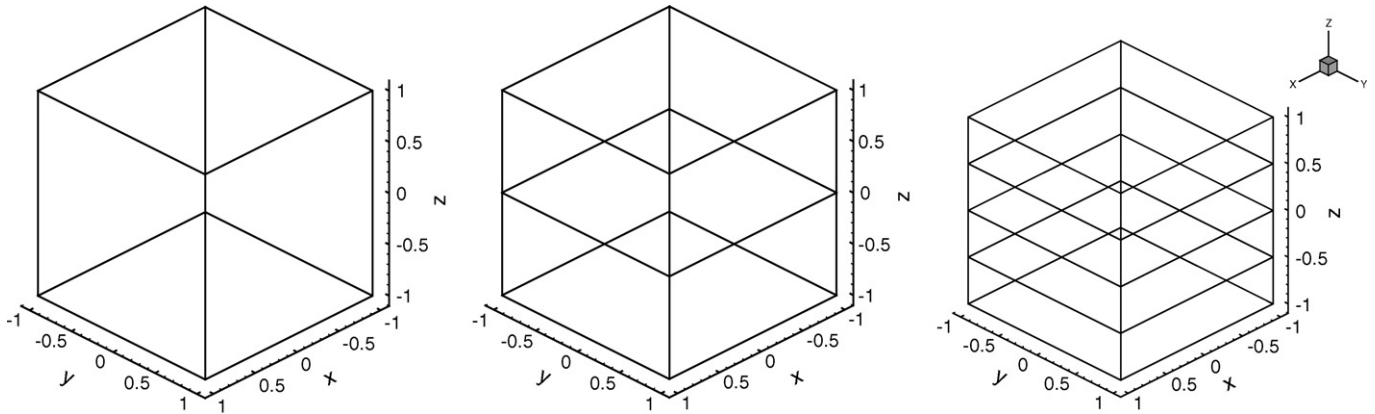
Fig. 2. The 1-, 2- and 4-element meshes used for the convergence studies of the R-R fluid. Each hexahedral element has a 10th order Jacobi polynomial approximating the solution in all three directions.

Reiner–Rivlin problem balanced by a body force is given by the one-component velocity field

$$\mathbf{U}(y, z) = \begin{pmatrix} (1 - z^2) \cos(\pi y) \\ 0 \\ 0 \end{pmatrix}, \quad P = 0, \tag{34}$$

together with the three-component, sustaining body force

$$\mathbf{F}(y, z) = \begin{pmatrix} \eta \cos(\pi y)(2 + \pi^2 - \pi^2 z^2) \\ -\pi\alpha \sin(2\pi y)(1 + z^2) \\ -2\pi^2 \alpha z(1 - z^2) \end{pmatrix}. \tag{35}$$

From Eq. (34) it is clear that the body force $\mathbf{F}(y, z)$ has but one component parallel to $\mathbf{U}(y, z)$ for the Newtonian case, and that the other two components which contain α are required to balance the nonlinear terms. The computational problem whose continuous solution is given by Eqs. (33) and (34) was set up for the meshes displayed in Fig. 2. For all of the computed velocity components and for the computed pressure Fig. 3 shows that the L_∞ error, relative to Eq. (33), has a clear monotonic dependence on α'. Furthermore, the effect of element boundaries has a secondary effect on the accuracy of the computed solution provided it converges. This is the main conclusion to be drawn from this test. For this problem convergence for multi-element meshes was limited to $\alpha' < 0.6$ whereas for the single element case convergence was attained at higher values. Convergence for this simple test flow is not an indicator of the level to be expected for the complex meshes described below. The pressure error, $\mathcal{O}(10^{-3})$ at $\alpha' \approx 0.8$, is 2 orders higher than the velocity error for this and all the examined values of α'.

5.2. Polynomial over-integration

Nonlinearities in the Reiner–Rivlin equation (23) contribute to the time-splitting scheme through the $\nabla \cdot \mathbf{C}$ term in Eq. (29) at every spatial integration point. In spectral/*hp* methods when the same integration rule is employed for both linear and nonlinear
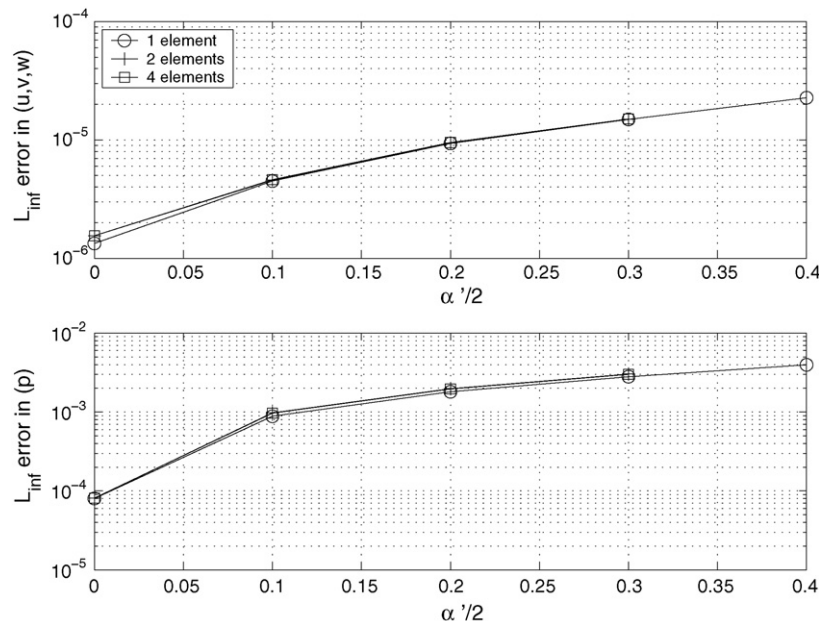

Fig. 3. L_∞ error relative to Eq. (34) for velocity (upper) and pressure (lower) plotted against the Deborah number as $\alpha'/2$ for 1-, 2- and 4-element meshes.

terms errors may occur for the latter from an insufficient number of quadrature points. A polynomial $u(\xi)$ of degree N is integrated exactly with $(N + 3)/2$ Gauss–Lobatto–Legendre quadrature points. The representation $u(\xi) = \sum_{i=0}^{N} \hat{u}\phi_i(\xi)$ in terms of basis functions $\phi_i(\xi)$ gives rise to inner products $\langle \phi_i(\xi)\phi_j(\xi) \rangle$ in the evaluation of quadratic nonlinearities. Let $M = N + 1$ be the number of modal coefficients for the polynomial expansion of $u(\xi)$, quadratic nonlinearities involve the computation of polynomials of degree $3N$ for which the minimum sufficient number of quadrature points is

$$Q_{3N} = \frac{3N + 3}{2} = \frac{3(M - 1) + 3}{2} = \frac{3M}{2}. \tag{36}$$

Studies of *over-integration* have been presented in [14] for the viscous Burger's equation; in this work over-integration is extended to the Reiner–Rivlin fluid. Fig. 4 shows the effect of the over-integration order (defined as the multiplicative factor of M in the right-hand side of (36)) on the velocity and pressure L_∞ error relative to the analytical solution for the meshes of Fig. 2. Integration accuracy of the quadratic nonlinearity of the Reiner–Rivlin terms is substantially improved with the *three-halves* rule; it increased by one order of magnitude in the velocity and pressure for the meshes of Fig. 2. The saturation of the error in the plot suggests that there is no numerical advantage in using more points; curiously, the accuracy in the pressure relative to that of the velocity component remains 2 orders of magnitude worse. However, this is also true for Stokes flow which suggests that the cause is not the non-Newtonian term.

6. Benchmark problem: parallel slot

For the rectilinear shear flow of a Newtonian fluid driven by a constant pressure gradient $\{P_x, 0, 0\}$ with components $\{u(y, z), 0, 0\}$, Kearsley [9] showed that the same velocity field

also satisfies the equilibrium problem for the Reiner–Rivlin stress with constant coefficients provided the pressure is defined by

$$P(x, y, z) = xP_x + \alpha \left(u\Delta^2 u - \frac{\omega^2}{2} \right), \quad \omega = \{0, u_z, u_y\}, \tag{37}$$

where the subscripts stand for the respective spatial derivatives, P_x is the constant driving pressure gradient, and Δ^2 is the Laplacian operator in the $\{y, z\}$ plane. In Poiseuille flow the term in α is constant, but in the general rectilinear flow this term gives rise to a pressure distribution within the $\{y, z\}$ plane. For the cross-section of Fig. 5 most of the pressure variation is confined to the junction of the channel with the slot.

From its definition, Eq. (10), the normalized hole pressure is obtained from Eq. (37) as

$$\frac{P_{\mathrm{H}}}{(\alpha\dot{\gamma}_{\mathrm{w}}^2)} = \frac{1}{2} - \frac{u_z^2}{8}. \tag{38}$$

Here the derivative u_z is taken at the midpoint of the slot's bottom. About one or two slot widths h from the bottom of a deep slot (Fig. 5) Poiseuille flow is obtained with maximum velocity $(h/H)^2$ times the corresponding value in the main channel. The hole pressure calculated relative to that point changes the last term in Eq. (38) to $-(h/H)^4/2$, which demonstrates that in this benchmark problem with $h/H = 1/10$ deviations from Kearsley's value of 1/2 for the normalized hole pressure are too small to be considered. Although Kearsley's problem is solvable in the y, z-plane it is converted here into a three-dimensional problem in a channel of finite length for the purpose of validation of the numerical code. The finite element mesh was constructed by replicating a constant *T-shaped* cross-section, Fig. 5, along the entire x-axis. As seen in the figure, the junction is a smooth quarter circle instead of a sharp edge. In order to simulate a
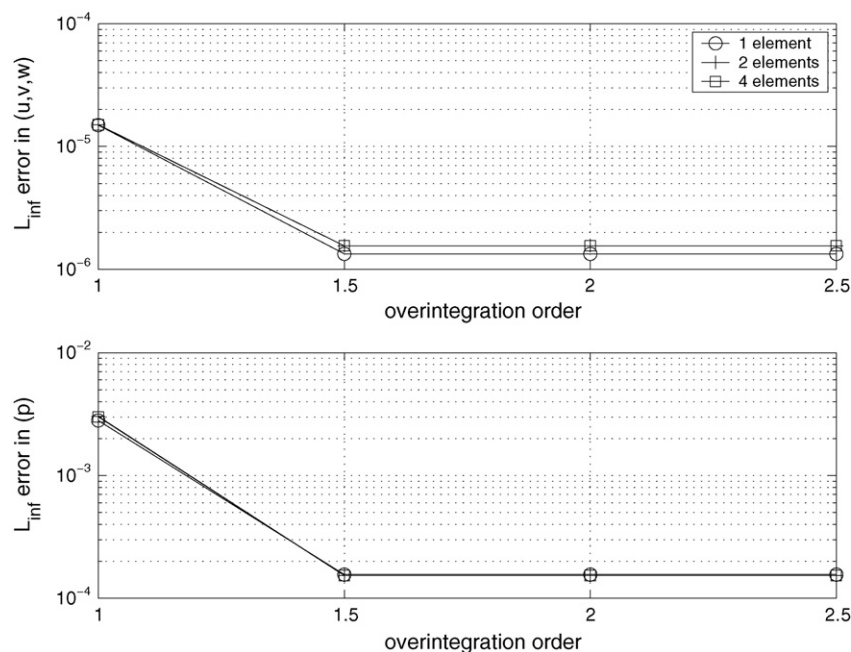

Fig. 4. L_∞ error relative to Eq. (34) for velocity (upper) and pressure (lower), at $\alpha' = 0.6$, plotted against the over-integration order for 1-, 2- and 4-element meshes.
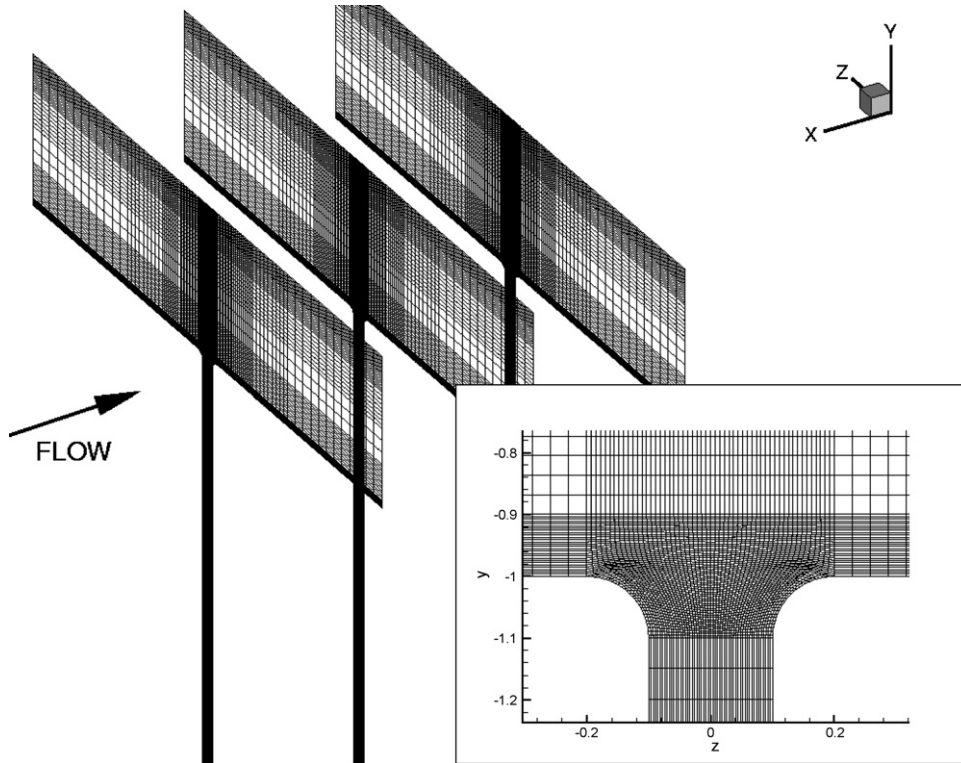
Fig. 5. Mesh used for Kearsley's parallel slot with detail of the rounded T-shaped cross-section.

channel of infinite length, the following boundary conditions were applied: at the far edges of the main channel, $z = \pm 3.5$, a Dirichlet parabolic profile $(1 - y^2, 0, 0)$ was imposed for the velocity, while on the entry and exit planes a Neumann boundary condition $\partial \mathbf{u}/\partial \mathbf{n} = 0$ was imposed. However, on the small part of the entry and exit planes close to the z-edges on either side, the combined condition $\partial \mathbf{u}/\partial \mathbf{n} = 0$, $P = 0$ ensured that the pressure at the channel edges would serve as a reference value. Moreover, a Dirichlet parabolic profile $(0.01 - z^2, 0, 0)$ was imposed for the velocity at the deep end of the slot. The flow was driven by a constant body force equivalent to the imposed driving pressure gradient P_x.

Meshes with rounded corners and sharp corners at the slot junction were tried. The rounded corners, combined with over-integration, gave r-values in closest agreement with Kearsley's [9] analytical value for deep, narrow holes. The calculated pressures along the centerline of the cross-section are displayed in Fig. 6 for several polynomial orders N. The approach to Kearsley's limit of 1/2 with increasing N was achieved only with over-integration using the *three-halves* rule, demonstrated above in Section 5.2. The inversion of the curves for $N = 3$ and 4 in Fig. 6 shows that the limit is not approached uniformly.

7. Numerical results for three-dimensional holes

With the walls of the plane channel of Fig. 1 at $y = \pm 1$, the fully three-dimensional hole problem is addressed with a prescribed Poiseuille velocity $u(y) = 1 - y^2$, $v = w = 0$ at the channel entrance, while the outflow channel boundary is pre-

scribed with the Neumann boundary condition $\partial \mathbf{u}/\partial n = 0$, $P = 0$. The boundaries for the cross-flow z-direction are assumed to be periodic, and zero velocities are prescribed on the remaining solid surfaces. A typical simulation for such a geometry has 2 million degrees of freedom. Results were obtained for polynomial orders $N = 2$ and 4 per direction, and no substantial differences were observed in the calculated fields.

The results for three-dimensional holes are presented in terms of the disturbance pressure field which is the extra pressure due
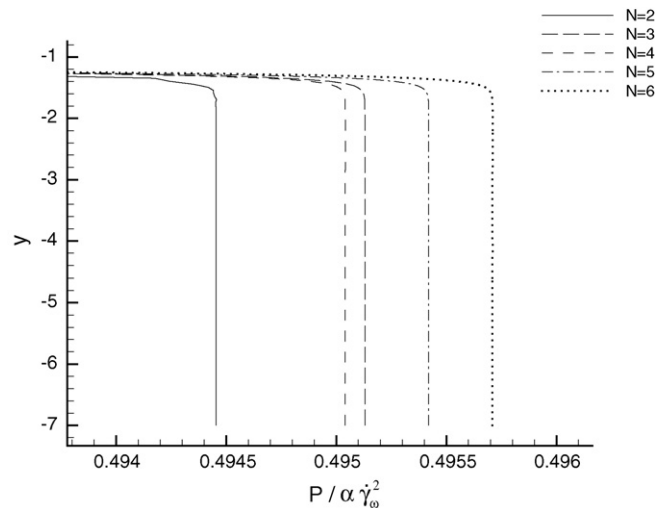

Fig. 6. Reiner–Rivlin disturbance pressures along the centerline of the cross-section for increasing polynomial order N, showing the approach to Kearsley's limit of 1/2 for $\alpha' = 0.1$. The lower wall of the main channel is at $y = -1$. Note that $\alpha \dot{\gamma}_w^2 = \alpha' \tau_w$.
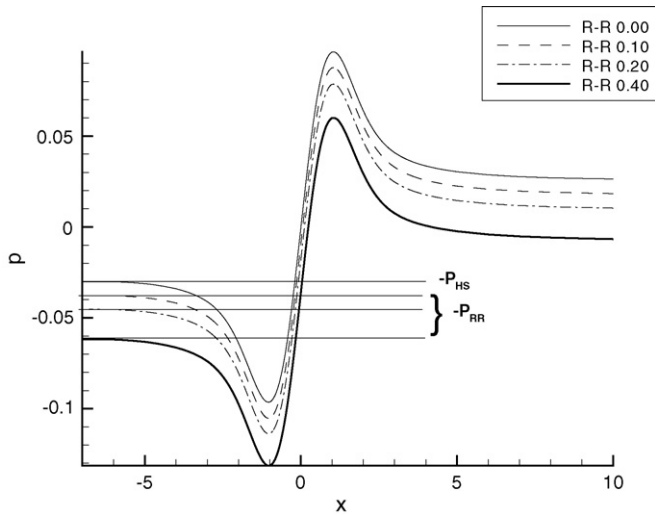
Fig. 7. Streamwise disturbance-pressure profiles along the centerline of the top wall, $b/H = 1$. The pressure constant is chosen so that the Reiner–Rivlin hole pressure can be read off from the negative of the intercept for each value of α' (indicated as R-R in the legend).

Fig. 8. Reiner–Rivlin hole pressure as a function of the Reiner–Rivlin number, α'.

to the disturbance created by the hole. Initially let the hole be covered by a membrane so that Poiseuille flow is obtained in the channel and within the hole the fluid is at rest. The initial pressure field is then a linear function of x in the channel and a constant in the hole. After the membrane is removed a new steady state is established. The difference between the final and initial pressure fields is the disturbance pressure. For the remainder of this section the disturbance pressure, scaled with τ_w, will be called simply the pressure, unless otherwise noted.

Fig. 7 shows the centerline pressure on the top wall of the channel for $b/H = 1$ for several values of α' (R-R). The pressure constant is chosen so that the pressure is zero at $(0, -d, 0)$, the center of the bottom plate of the hole at depth d. By definition (10) the far upstream ($x = -7$) value of the pressure is the negative of the hole pressure as indicated in Fig. 7, and the difference between the far downstream ($x = 10$) and far upstream values is the *pressure recovery* P_D due to reduced dissipation relative to the no-hole geometry. If P_H is added to each curve then the pressure will be zero far upstream, P_H at the bottom of the hole, and P_D far downstream. The advantage of setting the pressure to zero at the hole bottom is that P_H and P_D can be conveniently displayed on one plot. The plane $(0, y, z)$ is one of fore-aft symmetry since at each end of the channel the flow is asymptotic to Poiseuille flow. In Stokes flow the streamlines and the pressure field must then have fore-aft symmetry and anti-symmetry respectively as is evident in Fig. 7 and in Fig. 11 below and, furthermore, P_D must be equal to $-2P_H$. These properties of Stokes flow provide useful checks on the numerical solutions.

The Reiner–Rivlin hole pressures for three hole sizes are plotted in Fig. 8 according to Eq. (19), and rendered dimensionless with the Poiseuille wall shear stress, $\tau_w = \eta\dot{\gamma}_w$. The linearity of the plots suggests that for Reiner–Rivlin numbers less than about 0.4 the solutions obtained here fall within the domain of first order perturbations of Stokes flow. In both theoretical and experimental work it has been assumed [7,8] that the hole pressure in Stokes flow is negligible compared to
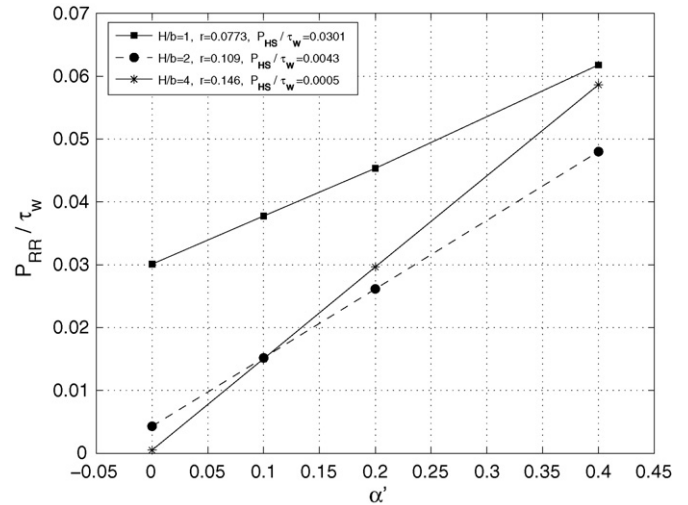
non-Newtonian effects. For large holes the experimental data of Tong [15] for $b/H = 1$ show P_{HS} to be measurable. Over the range of numerical values in Fig. 8. P_{HS} scales roughly as $\sim (b/H)^3$ while r scales as $\sim (b/H)^{-1/2}$. The latter is unlikely to hold for very small b/H, and the r values given here may be approaching the Higashitani–Pritchard [10] value of 1/6 as $b/H \to 0$; indeed a calculation for $b/H = 1/10$ on a coarse mesh gave $r = 0.17$. Kearsley's value of 1/2 for the parallel slot may well be an upper bound for r.

When the pressure curves in Fig. 7 are shifted by $P_{RR} - P_{HS}$ the result is essentially a single curve as shown in Fig. 9 for $b/H = 1/2$; similar results were obtained for all values of b/H. This plot shows that away from the aperture the pressure distribution for $\alpha' > 0$ differs from the corresponding Stokes field by a constant. This implies that far from the aperture the flow is governed by the Stokes equation. However, it is clear from Figs. 7 and 9 that, except for very small values of b/H, the flow near the wall opposite the hole is not undisturbed
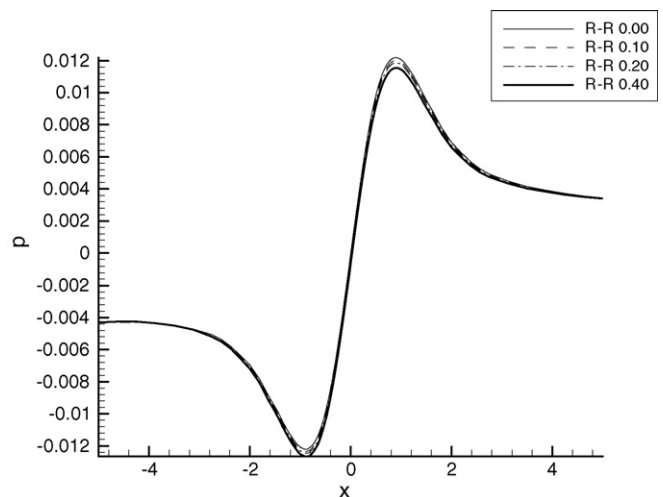

Fig. 9. Centerline disturbance pressure profiles of Fig 7 shifted upwards by $P_{RR} - P_{HS}$ for $b/H = 1/2$ onto a single curve for α' (R-R in the legend) up to 0.4.
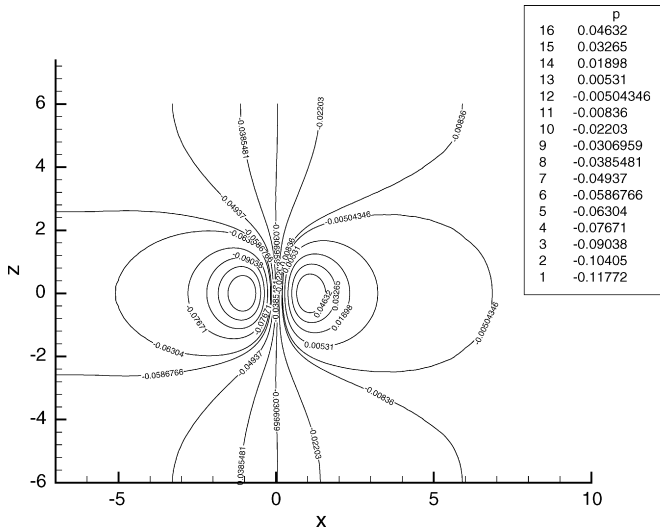
Fig. 10. Disturbance-pressure contours on the top plane, $b/H = 1$, $\alpha' = 0.4$ showing that the disturbance extends across the entire channel width; positive contours lie to the right of $x = 0$.

Fig. 11. Three-dimensional pathlines at a small distance above the wall for $\alpha' = 0$.

Poiseuille flow as assumed in the Higashitani–Pritchard [10] theory. While the shifted pressure profiles differ slightly near their maximum/minimum values, they coincide very closely as they level off downstream. This means that P_D remains at the Stokes value even though P_H does not.

Fig. 10 displays pressure field contours for $\alpha' = 0.4$ on the top wall $(x, H/2, z)$ for $b/H = 1$. The contour pattern shows the unexpected result that the hole disturbance of $O(P_H)$ extends all the way across the channel. Since P_{HS} scales as $(b/H)^3$ it suggests that in experimental designs featuring large holes, such as the Lodge and Vargas [7] stressmeter, the placement of transducers to measure the gradient of the total pressure will be subject to systematic error in the arrangement shown in Fig. 1. Furthermore, a lateral off-set of the transducer T_1 does not resolve the problem; clearly, it should be placed upstream in the undisturbed region.

The hole-pressure is an example of how the asymmetry of an apparently small geometric disturbance of a viscometric domain can give rise to a significant effect due mostly to the normal stresses. For the values of α' of this work the velocity fields differ only slightly from their Newtonian counterparts. In Fig. 11
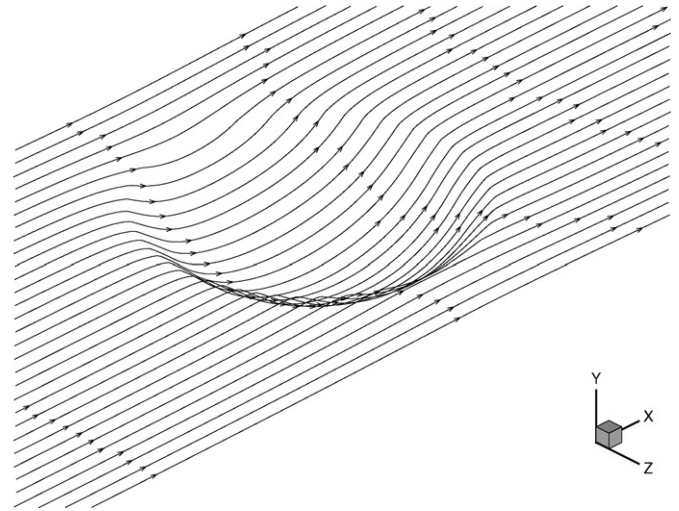
streamlines originating upstream at a distance $0.025H$ from the lower wall are seen to form a bowl as they pass over the aperture with $\alpha' = 0$. This picture changes very slightly when α' is increased to 0.4, and examination of the velocity field through most of the domain yields a similar conclusion. This is consistent with Fig. 9 which shows the pressure field on the top wall to be Stokesian, but it does not account for the extra hole pressure which shifts the pressure curves onto a single one. The plane of the aperture is the one location where the Reiner–Rivlin velocity fields are distinctly different from their Newtonian counterparts. In Fig. 12 the velocity components are plotted in the plane of the aperture along $(0, -H/2, z)$, for $b/H = 1$ and $\alpha' = 0.4$. The Newtonian v, w-components, by symmetry, are zero while their Reiner–Rivlin counterparts are small but distinct from the numerical errors. When the u-components are magnified they exhibit differences of the same magnitude as the Reiner–Rivlin v, w-components. Thus even in the limit of small shear rates the three-dimensional hole-pressure flow in the region of the aperture is considerably more complicated than the corresponding two-dimensional problem. The Higashitani–Pritchard [10] theory is built conceptually on the assumption that the aperture region has streamlines in the pattern of Fig. 11.
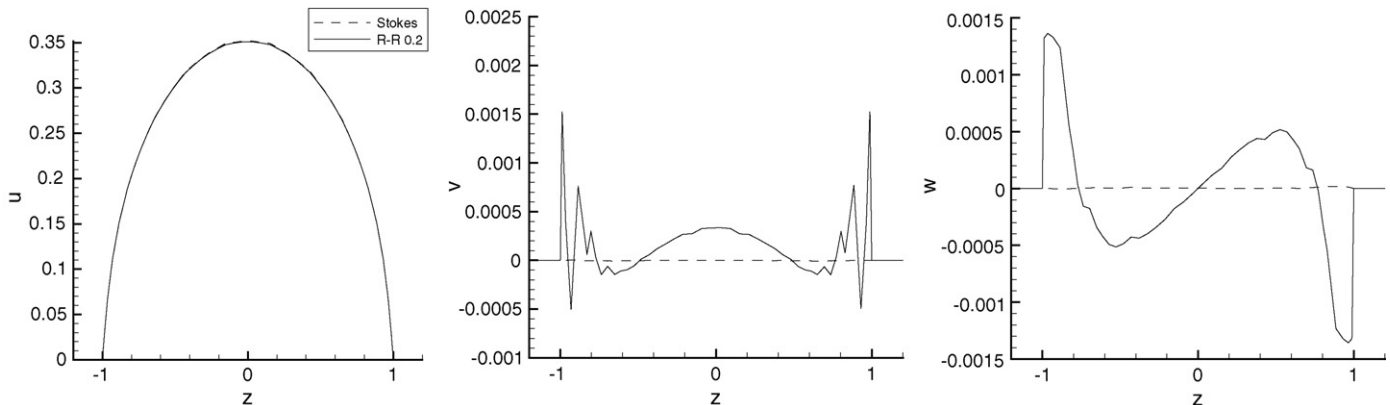

Fig. 12. Velocity components across the aperture for $\alpha' = 0.4$, showing that v, w are 2 orders smaller than u.

8. Conclusion

The low shear-rate hole pressure for a non-Newtonian fluid has been shown to be determined by the augmented second order fluid, Eq. (9), derived from the materially constant stress, Eq. (3), in which the Reiner–Rivlin stress has constant coefficients η, and α. In that equation the definition of the isotropic stress allows the equilibrium equation to be satisfied by the solution of the Reiner–Rivlin problem, Eq. (4), by means of Theorem 1.1 proved by Caswell [1]. This reduction in the order of spatial derivatives is numerically advantageous, and naturally breaks the problem into two steps. In the first, the hole pressure relative to the Reiner–Rivlin value is determined analytically to be independent of hole size and to be the same as the Tanner and Pipkin [8] result for two-dimensional slots. In step two the Reiner–Rivlin value is determined by solution of Eq. (4). Since the term in α in Eq. (1) plays no role in plane flow, the Reiner–Rivlin stress has been put into a form, Eq. (23), that is unaffected by the small discrepancies in the dilatation rate $\nabla \cdot \mathbf{V}$ from zero which occur in numerical simulation. This avoids the creation of artificial three-dimensional forces in regions of plane flow embedded in a three-dimensional domain. Our modified $\mathcal{N}\varepsilon\kappa\mathcal{T}\alpha r$ code was checked in two benchmark problems with known analytical solutions. In particular, for Kearsley's [9] parallel slot the r coefficient in Eq. (19) is calculated to within less than 1% of the analytical value of $1/2$. For the slot, over-integration was found to be essential to obtain convergence with respect to the spectral order N.

The numerical values of the Reiner–Rivlin hole pressure have been shown to follow Eq. (19), and its constants P_{HS}, and r have been tabulated for $b/H = 1/4, 1/2, 1$. The Stokes hole pressure, P_{HS}, has been shown to scale roughly as $(b/H)^3$, and from the experimental data of Tong [15] its magnitude at $b/H = 1$ was found to be in the measurable range. The coefficient r of the Reiner–Rivlin number which determines hole size dependence of the total hole pressure P_{H} in Eq. (20) is smaller than the Higashitani–Pritchard [10] value of $1/6$, which may be the limit for very small holes. Of value to experimental design is the observation that the pressure on the channel wall opposite the aperture is significantly disturbed. An important assumption of the Higashitani–Pritchard theory is that this disturbance is negligible, which is true only for very small holes. This assumption has been influential in the design of the Lodge stressmeter where the hole pressure was measured with pressure transducers located opposite the aperture and at the bottom of the hole. This transducer together with one located upstream, as in Fig. 1, was also used to measure the pressure gradient of the undisturbed channel flow. This apparent hole pressure will be exactly zero in Stokes flow due to its symmetry properties, but, once nonlinear effects such as non-Newtonian stresses or inertia are significant, the measurement cannot be accurately interpreted. Furthermore, the measured pressure gradient will not be the undisturbed value. As might be expected, large holes are intrusive, and their disturbance, as shown in Fig. 10, can reach all the way across the channel.

Appendix A

In Cartesian coordinates $\{x, y, z\}$ the velocity field has components $\{u, v, w\}$, and with subscripts to denote the spatial derivatives the components of $\mathbf{B}$ can be arrayed as,

$$\mathbf{B} = \begin{pmatrix} u_x - v_y - w_z & u_y + v_x & u_z + w_x \\ * & v_y - u_x - w_z & v_z + w_y \\ * & * & w_z - u_x - v_y \end{pmatrix} \quad (A.1)$$

The components of $\mathbf{B}^2$ are then

$$\begin{aligned} B^2_{\langle xx\rangle} &= (u_x - v_y - w_z)^2 + (u_y + v_x)^2 + (u_z + w_x)^2, \\ B^2_{\langle xy\rangle} &= (u_z + w_x)(v_z + w_y) - 2w_z(u_y + v_x), \\ B^2_{\langle xz\rangle} &= (u_y + v_x)(v_z + w_y) - 2v_y(u_z + w_x), \\ B^2_{\langle yy\rangle} &= (u_y + v_x)^2 + (v_y - u_x - w_z)^2 + (v_z + w_y)^2, \\ B^2_{\langle yz\rangle} &= (u_y + v_x)(u_z + w_x) - 2u_x(v_z + w_y), \\ B^2_{\langle zz\rangle} &= (u_z + w_x)^2 + (v_z + w_y)^2 + (w_z - u_x - v_y)^2. \end{aligned} \quad (A.2)$$

It can be shown that

$$\frac{1}{2}[\operatorname{tr}\mathbf{B}^2 - (\operatorname{tr}\mathbf{B})^2]$$

$$= (\nabla \cdot \mathbf{V})^2 + \omega^2 - 4\left[\frac{\partial(u, w)}{\partial(x, z)} + \frac{\partial(u, v)}{\partial(x, y)} + \frac{\partial(v, w)}{\partial(y, z)}\right], \quad (A.3)$$

where ω is the magnitude of the vorticity vector

$$\omega = \{\omega_{\langle x\rangle}, \omega_{\langle y\rangle}, \omega_{\langle z\rangle}\} = \{w_y - v_z, u_z - w_x, v_x - u_y\}. \quad (A.4)$$

From Eq. (23) the components of $\mathbf{C}$ can now be written as

$$C_{\langle xx\rangle} = -\omega^2_{\langle x\rangle} + 4\frac{\partial(v, w)}{\partial(y, z)},$$

$$C_{\langle xy\rangle} = -\omega_{\langle x\rangle}\omega_{\langle y\rangle} + 2\frac{\partial(w, v)}{\partial(x, z)} + 2\frac{\partial(w, u)}{\partial(y, z)},$$

$$C_{\langle xz\rangle} = -\omega_{\langle x\rangle}\omega_{\langle z\rangle} + 2\frac{\partial(v, w)}{\partial(x, y)} + 2\frac{\partial(u, v)}{\partial(y, z)},$$

$$C_{\langle yy\rangle} = -\omega^2_{\langle y\rangle} + 4\frac{\partial(u, w)}{\partial(x, z)},$$

$$C_{\langle yz\rangle} = -\omega_{\langle y\rangle}\omega_{\langle z\rangle} + 2\frac{\partial(v, u)}{\partial(x, z)} + 2\frac{\partial(w, u)}{\partial(x, y)},$$

$$C_{\langle zz\rangle} = -\omega^2_{\langle z\rangle} + 4\frac{\partial(u, v)}{\partial(x, y)}. \quad (A.5)$$

If the three-dimensional field contains embedded, two-dimensional regions such as a plane of symmetry, where $w = 0$, and all derivatives $\partial(*)/\partial z = 0$, then inspection of Eq. (A.5) confirms that all components of **C** are identically zero, except

$$C_{\langle zz \rangle} = -\omega_{\langle z \rangle}^2 + 4 \frac{\partial(u, v)}{\partial(x, y)}. \tag{A.6}$$

With the cross-plane gradient $\partial(C_{\langle zz \rangle})/\partial z$ being zero, $C_{\langle zz \rangle}$ has no dynamic effect. This result is independent of the magnitude of $(\nabla \cdot \mathbf{V})$. Eq. (A.5) are the same as they would be in the **A**-formulation with exact incompressibility.

References

[1] B. Caswell, Non-Newtonian flow at lowest order: the role of the Reiner–Rivlin stress, J. Non-Newton. Fluid Mech. 133 (1) (2006) 1–13.

[2] W.O. Criminale, J.L. Ericksen, G. Filbey Jr., Steady flow of non-Newtonian fluids, Arch. Ration. Mech. 1 (1958) 410–417.

[3] M.W. Johnson Jr., Some variational theorems for non-Newtonian flow, Phys. Fluids 3 (1961) 871–878.

[4] R.I. Tanner, Some extended Giesekus-type theorems for non-Newtonian fluids, Rheol. Acta 28 (1989) 449–452.

[5] H. Giesekus, Die Simultane Translations und Rotationsbewegung einer Kugel in einer Elastoviskosen Flüssigkeit, Rheol. Acta 3 (1963) 59–71.

[6] R.I. Tanner, Plane creeping flows of incompressible second order fluids, Phys. Fluids 9 (1966) 1246.

[7] A.S. Lodge, L. de Vargas, Positive hole pressures and negative exit pressures generated by molten polyethylene flowing through a slit die, Rheol. Acta 22 (1983) 151–170.

[8] R.I. Tanner, A. Pipkin, Intrinsic errors in pressure-hole measurements, Trans. Soc. Rheol. 14 (1969) 471.

[9] E.A. Kearsley, Intrinsic errors for pressure measurements in a slot along a flow, Trans. Soc. Rheol. 14 (3) (1970) 419–424.

[10] K. Higashitani, W.G. Pritchard, A kinematic calculation of intrinsic errors in pressure measurements made with holes, Trans. Soc. Rheol. 16 (4) (1972) 687–696.

[11] G.E. Karniadakis, M. Israeli, S.A. Orszag, High-order splitting methods for incompressible Navier–Stokes equations, Journal of Computational Physics 97 (1991) 414.

[12] G.E. Karniadakis, S.J. Sherwin, Spectral/*hp* Element Methods for CFD, Oxford University Press, 1999.

[13] G.-S. Karamanos, C. Evangelinos, R.M. Kirby, G.E. Karniadakis, DNS of turbulence on a PC/Linux cluster: fact or fiction? in: Proceedings of the SuperComputing, 1999.

[14] R.M. Kirby, Toward dynamic spectral/*hp* refinement: algorithms and applications to flow-structure interactions. Ph.D. Thesis, Brown University, 2003.

[15] P.P.-L. Tong, Fundamental studies on a laboratory stressmeter. Ph.D. Thesis, University of Wisconsin-Madison, 1980.